Multiscale multifractal detrended-fluctuation analysis of two-dimensional surfaces

Fang Wang

College of Science, Hunan Agricultural University, Changsha, P. R. China

Qingju Fan[*]

Department of Statistics, School of Science, Wuhan University of Technology, Wuhan, P. R. China

H. Eugene Stanley

Center for Polymer Studies and Department of Physics, Boston University, Boston, Massachusetts 02215, USA

Two-dimensional (2D) multifractal detrended fluctuation analysis (MF-DFA) has been used to study monofractality and multifractality on 2D surfaces, but when it is used to calculate the generalized Hurst exponent in a fixed time scale, the presence of crossovers can bias the outcome. To solve this problem, multiscale multifractal analysis (MMA) was recent employed in a one-dimensional case. MMA produces a Hurst surface $h(q,s)$ that provides a spectrum of local scaling exponents at different scale ranges such that the positions of the crossovers can be located. We apply this MMA method to a 2D surface and identify factors that influence the results. We generate several synthesized surfaces and find that crossovers are consistently present, which means that their fractal properties differ at different scales. We apply MMA to the surfaces, and the results allow us to observe these differences and accurately estimate the generalized Hurst exponents. We then study eight natural texture images and two real-world images and find (i) that the moving window length (WL) and the slide length (SL) are the key parameters in the MMA method, that the WL more strongly influences the Hurst surface than the SL, and that the combination of WL = 4 and SL = 4 is optimal for a 2D image; (ii) that the robustness of $h(2,s)$ to four common noises is high at large scales but variable at small scales; and (iii) that the long-term correlations in the images weaken as the intensity of Gaussian noise and salt and pepper noise is increased. Our findings greatly improve the performance of the MMA method on 2D surfaces.

I. INTRODUCTION

The fractal and multifractal theory developed by Mandelbrot [1,2] has produced new ways of understanding image analysis. We now see that there is a connection between the gray value of an image and fractals in nature, that most natural surfaces are spatially isotropic fractals, and that their intensity images are fractal or multifractal [3].

In traditional multifractal analysis (MFA), the concept of multifractal dimension is a powerful tool for describing both the local and global structure of irregular objects and their overall self-similarity. Its ability to characterize image roughness is also consistent with the basic operation of the human vision system [3]. MFA can also capture the scaling of fluctuations, the mutation of gray levels, self-similarity, change of phase, and frequency. This advanced tool can thus be used to solve various traditional image processing problems, e.g., recognizing heterogeneity in medical images [4], detecting decay in log cross-section images [5], and targeting the location of remote sensing images [6]. Many existing MFA techniques are limited to stationary object measurements, however, and cannot deal with those that are nonstationary. To overcome this inability, detrended fluctuation analysis (DFA), in which certain trends hidden in the object are eliminated, has been developed [7]. The performance of the DFA has been proved to be superior to the wavelet method when dealing with the nonstationary multifractal measure [8]. Both DFA

and its multifractal version (MF-DFA) [9] have been used to resolve various nonstationary time series in many research fields [10–14]. Because real-world images may also embody nonstationary measures, one-dimensional (1D) MF-DFA has been extended to the two-dimensional (2D) case. Gu and Zhou [15] proposed the 2D version of MF-DFA in 2006, and the new method was adopted by a number of other researchers to carry out 2D surface analysis [16–22]. Yadav *et al.* [19] used 2D MF-DFA to analyze AFM images of the surface morphologies of LiF thin films. Wang *et al.* used a global and local generalized Hurst exponent obtained by 2D MF-DFA to delineate lesions in six corn disease leaf images [20] and to identify tree species from 15 different leaf images [21]. Yu *et al.* [22] applied a new 2D MF-DFA-based segmentation method to locate and segment tumor regions from magnetic resonance images. These results strongly indicate that 2D MF-DFA is a powerful tool for uncovering multifractality in 2D surfaces.

When MF-DFA is used to analyze the multifractal scaling of an object's fluctuations, the method can assume scales that exceed the overall size of the studied object. Thus crossovers [13,23] can appear in the double-log plot of the fluctuation function $F_q(s)$ versus scale s in standard MF-DFA, e.g., the slope of the fluctuation functions can change at some special scale. Because of multiple measures with different properties, these crossovers can occur within a particular scaling range in a time series or a 2D surface and produce biased results. Solving for the 1D case, Stanley *et al.* used a local Hurst exponent based on the DFA method to analyze a heart rate series [24]. Grech and Mazur did the same for

---
[*]fanqingju@hotmail.com

a stock price series [25]. In like manner Echeverria *et al.* used an $\alpha\beta$ filter based on the Kalman filter to estimate local exponents and analyze human cardiac data [26]. Govindan *et al.* quantified the long-range correlation of short fetal cardiac data sets by computing the mean value of the local exponents associated with the phase randomized surrogate technique [27]. Castiglioni *et al.* estimated the temporal spectrum of scale exponents $\alpha_{\mathrm{DFA}}(s)$ in their study of heart rate variability and blood pressure [28,29]. All of these studies use the monofractal DFA method but do not define fixed scale ranges and instead vary the scales along the $F_q(s)$ results when producing the local DFA exponent $\alpha_{\mathrm{DFA}}(s)$, thereby accessing the multiple properties caused by the differing scales. Gieraltowski *et al.* [30] further this approach by proposing multiscale multifractal analysis (MMA), which has a spectrum with variable scale ranges and provides complete information about fractal properties along the entire time scale. This approach has also been used to solve problems associated with traffic flow [31] and heart rate variability [32]. These successful results indicate that MMA is workable for solving 1D series problems. Whether this is true for the 2D case is yet to be verified.

Our goal here is to validate the MMA method for 2D surfaces and explore the factors that potentially influence the method. Section II describes the 2D version of MF-DFA and MMA. Section III describes and discusses our approach. We examine the universality of multiple scales on a 2D surface, validate the 2D MMA method for 2D monofractal synthetic surfaces, and do the same for the multifractal, stationary, and nonstationary cases. We investigate the impact of two key parameters on the 2D MMA method using eight natural texture images, and we use real-world images to examine how noise affects 2D MMA. Section IV provides a brief summary of our study.

II. METHODS

A. 2D MF-DFA

We expand the 1D MF-DFA by Gu and Zhou [15] into a 2D version by calculating the $h(q)$ exponents and measuring the long-term correlation of gray values. We find a self-similar surface represented by an $M \times N$ matrix $X = X(i,j)$, $i = 1,2,\ldots,M$ and $j = 1,2,\ldots,N$. We partition it into a $M_s \times N_s$ nonoverlapping square subsurface of equal length s, where $M_s \equiv \mathrm{int}(M/s)$ and $N_s \equiv \mathrm{int}(N/s)$ are positive integers. Each subsurface is denoted by $X_{m,n} = X_{m,n}(i,j)$ with $X_{m,n}(i,j) = X(r+i,t+j)$ for $1 \leqslant i,j \leqslant s$, where $r = (m-1)s$ and $t = (n-1)s$. Because M and N are not multiples of the length s, we ignore the subsurfaces in the upper right and the bottom. We repeat the partitioning procedure starting from the other three corners and determine the cumulative sum of each subdomain $G_{m,n}(i,j) = \sum_1^i \sum_1^j X_{m,n}(k_1,k_2)$. For each surface $G_{m,n}$ we obtain a local trend $\widetilde{G}_{m,n}$ by fitting it with a prechosen bivariate polynomial function. The residual matrix is then given by $y_{m,n}(i,j) = G_{m,n}(i,j) - \widetilde{G}_{m,n}(i,j)$. We then define the detrended fluctuation function $F(m,n,s)$ for the segment $X_{m,n}$ to be

$$F^2(m,n,s) = \frac{1}{s^2} \sum_{i=1}^{s} \sum_{j=1}^{s} y_{m,n}(i,j)^2. \qquad (1)$$

We average over all subsurfaces to obtain the qth-order average fluctuation function

$$F_q(s) = \left\{ \frac{1}{M_s N_s} \sum_{m=1}^{M_s} \sum_{n=1}^{N_s} [F(m,n,s)]^q \right\}^{1/q}, \qquad q \neq 0, \quad (2)$$

$$F_q(s) = \exp\left\{ \frac{1}{M_s N_s} \sum_{m=1}^{M_s} \sum_{n=1}^{N_s} \ln[F(m,n,s)] \right\}, \qquad q = 0 \quad (3)$$

Finally, we vary the value of s to get a series of $F_q(s)$. If there is a long-range power-law correlation for large values of s, then

$$F_q(s) \propto s^{h(q)}. \qquad (4)$$

This allows us to obtain the scaling exponent $h(q)$ via linearly regressing $\log F_q(s)$ on $\log s$. The $h(q)$ is the so-called generalized Hurst index. The $h(q = 2)$ can be related to the Hurst exponent H of the surface directly, i.e., $h(q = 2) = H$ for the stationary surface and $h(q = 2) = H + 2$ for the nonstationary signal [33]. In addition, if the $h(q)$ is dependent on q, the surface is considered multifractal; if not, it is monofractal. In general, the $h(q)$ plot for $q < 0$ refers to those subsurfaces with a low variance (small fluctuations) of $F_q(s)$, while for $q > 0$ the plot characterizes the subsurfaces with a large variance (large fluctuations). Note that when q is positive, $h(q)$ yields more stable results.

Note that we use a local trend $\widetilde{G}_{m,n}$ to determine the detrended fluctuation function. Using Zhou *et al.* [33], we set the quadratic trending function to be $\widetilde{G}_{m,n}(i,j) = ai^2 + bj^2 + cij + di + ej + f$, where a, b, c, d, e, and f are free parameters to be determined by the least-squares method. Note also that when we calculate the family of curves $F_q(s)$ we must choose an appropriate range for scale s. If we do not choose an appropriate range the fitting exponent will be biased. If s is too large, the division of the time series will produce too few windows. If s is too small, the detrending procedure will be executed on a set of points too few in number. Drawing on 1D research [30,31] and previous 2D research [17,21], we set the usable range of scales in this work to be $s \in [6,\min(M,N)/4]$ with 20 isometrics in the logarithmic coordinates, where (M,N) is the size of the surface.

B. Multiscale MF-DFA

Because the single scaling exponent $h(q)$ may be missing important information associated with different scales, we propose using multiscale multifractal analysis (MMA) [30] in which the local scaling exponent is on certain scales of the MF-DFA. This 2D MMA uses a series of $h(q)$ in all the local scale ranges instead of a single series produced using standard MF-DFA. We use MF-DFA to calculate all $F_q(s)$ and sweep through the entire range of scale s along the $F_q(s)$ plot with a moving fitting window. In each window we calculate the local scaling exponent from the slope of the fitting line between the $\log[F_q(s)]$ and $\log(s)$ belonging to the window. We thus obtain the entire temporal spectrum of scale exponents, which allows us to study the quasicontinuous changes in the $h(q)$ dependence versus the range of scale s and to obtain the generalized dependence $h(q,s)$ (the Hurst surface). On the Hurst surface, the $h(q,s)$ embodies the
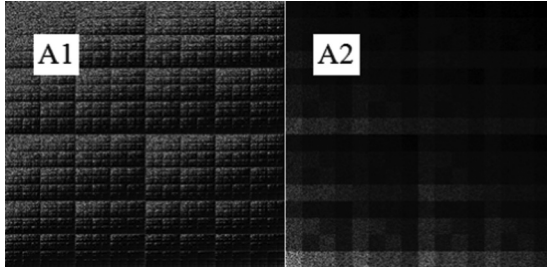
FIG. 1. Two samples of synthetic surfaces merged by 2D multifractal signals and uniformly distributed random noises.

long-term correlation of gray values on a 2D surface at all scales, which yields information about the fluctuation levels at the different frequency bands. As an important notion worthy of mentioning, our Hurst surface is calculated by using identical scales' range regardless of the potential of different multiscale properties which exist in the orthogonal directions of the 2D surface, in other words, our generative mechanism of the Hurst surface is an approximation when analyzing a 2D surface.

The fit is made only for points currently inside the moving window. The calculated $h(q,s)$ is highly dependent on two factors: (i) the length of the moving fitting window (WL) and (ii) the slide length (SL). Because the fluctuation functions $F_q(s)$ are presented in double-log coordinates, the moving fitting window expands logarithmically and seems to be of constant width. Its length determines the number of scales s and corresponding $F_q(s)$ in each window, which refers to the fitting accuracy of the $h(q,s)$. The SL gives the shift length of windows and determines the number of the local $h(q)$, which refers to the shape of the Hurst surface. We investigate how the WL and SL affect the 2D MMA method in Sec. III 3. On a 2D surface of size 512×512 we assign the values WL $= 4$ and SL $= 4$. The starting window includes scale $s \in [6,24]$, the second subwindow includes scale $s \in [10,40]$, and then we move and expand it to reach the final subwindow $s \in [30,120]$ [see Fig. 2(b)]. We use the center point of the Hurst surface to calibrate the scale axis in each fitting window, i.e., we begin at $s = 15$ (the center point of the first subwindow $s \in [4,24]$) and end at $s = 75$ (the center point of the final subwindow $s \in [30,120]$). Note that we use a linear axis on the Hurst surface. This differs from the plot of $F_q(s)$ versus s, which uses a logarithmic axis for the scale s.

III. RESULTS AND DISCUSSION

A. The universality of the multiple scales in 2D surface

To describe the different multifractal properties that occur at different scales [i.e., how $h(q)$ is oscillatory at different scales], we use 2D measurements to merge the results of two tests of a synthetic surface. We first use multiplicative cascading to create a multifractal surface. We begin by partitioning a square into four subsquares of the same size. We then assign four measurement proportions p_1, p_2, p_3, and p_4 (subject to $p_1 + p_2 + p_3 + p_4 = 1$, here we set $p = [p_1, p_2, p_3, p_4]$ $= [0.1, 0.2, 0.3, 0.4]$). Each subsquare is further partitioned into four smaller squares, and the measurement is reassigned
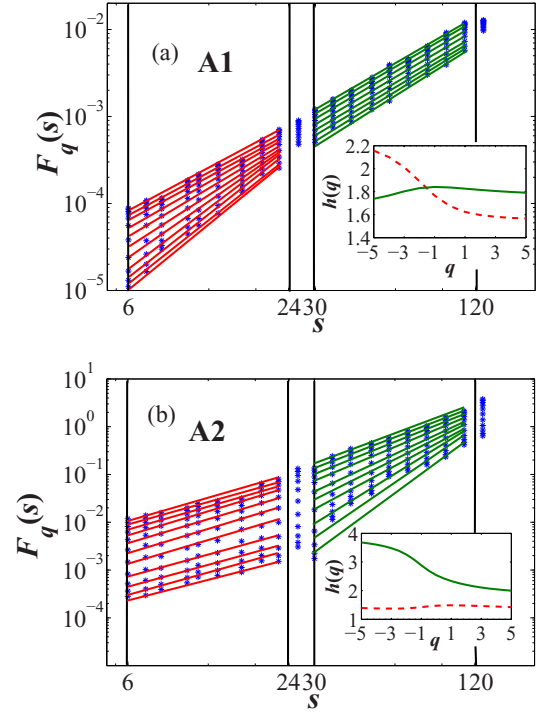

FIG. 2. Multifractal structures of the merged surfaces. The main panel is the $F_q(s)$ versus s in double-log plot. The vertical lines show two examples of the fitting windows for the small scales $s \in [6,24]$ and the large scales $s \in [30,120]$. Inset is the $h(q)$ curves calculated for the small (red dash line) and for the large scales (green solid line).

with the same proportions. The procedure is repeated nine times, and the result is a 2D multifractal measurement of size 512×512 pixels. In the first test, according to Ref. [30], we remove all values < 0.000001 from this multifractal surface
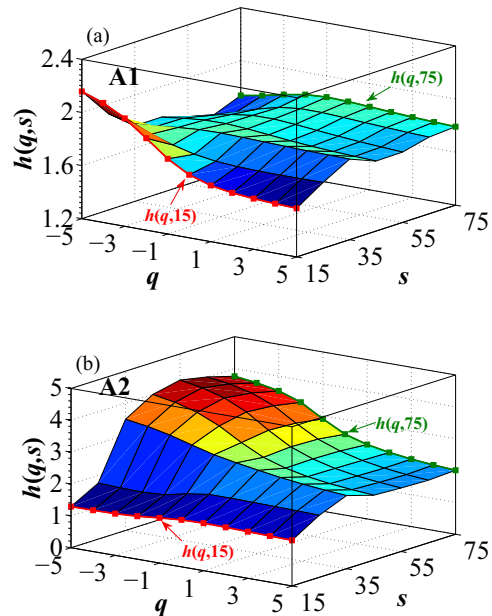

FIG. 3. Hurst surface $h(q,s)$ dependence calculated for the surfaces A1 and A2 with WL $= 4$ and SL $= 4$.
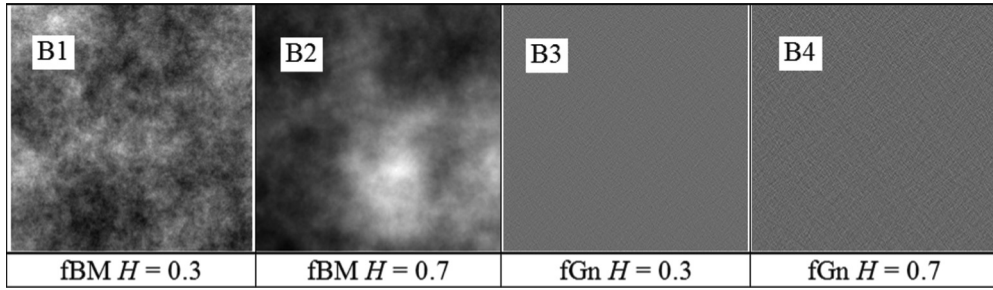
FIG. 4. 2D synthetic fractal surfaces generated by fBM model and fGn model with known Hurst exponents.

so that only a few of the largest elements are left. In their place, we substitute uniformly distributed random numbers from the range [0, 0.0001] (similar to the largest values in the quadrinomial cascade). We obtain a quadrinomial cascade surface embedded in random noise (see A1 on the left side of Fig. 1). We analyze this 2D signal and find it is multifractal at small scales but monofractal at larger scales because of the

effect of noise. Figure 2(a) shows its multifractal structure; Fig. 2(b) shows a multiplicative cascading process with $p = [0.1, 0.2, 0.3, 0.4]$ that produces a multifractal surface of size 16×16 and then replaces every point x_{ij} with 1024 points (forming a matrix of 32×32) generated using the formula $x_{ij}r$, where r denotes a uniformly distributed random number from the range [0, 3]. We thus obtain another surface of quadrinomial cascade embedded in random noise (see A2 on
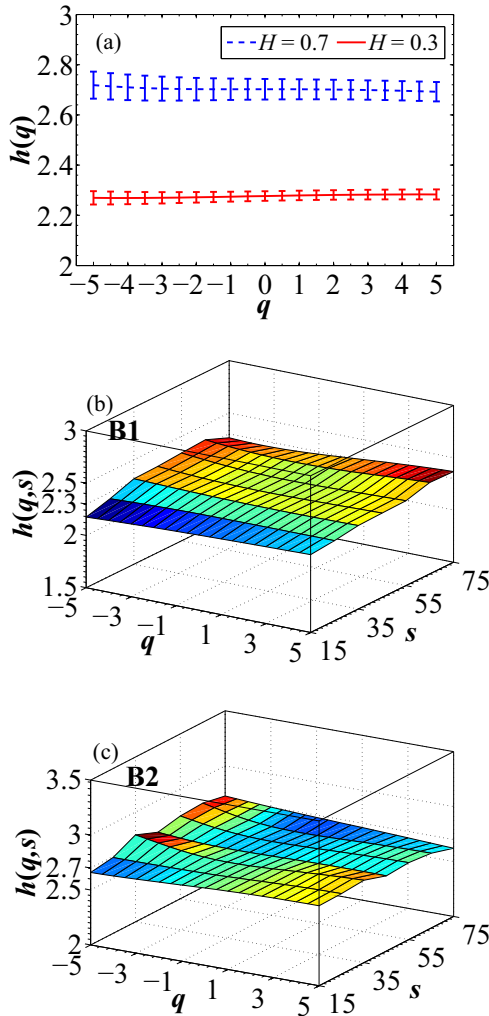

FIG. 5. Estimated multifractal long range correlation scaling exponents for the fBm surfaces B1 and B2 with given Hurst indices H. Error bars indicate standard deviation calculated from 20 independent realizations of the corresponding processes.
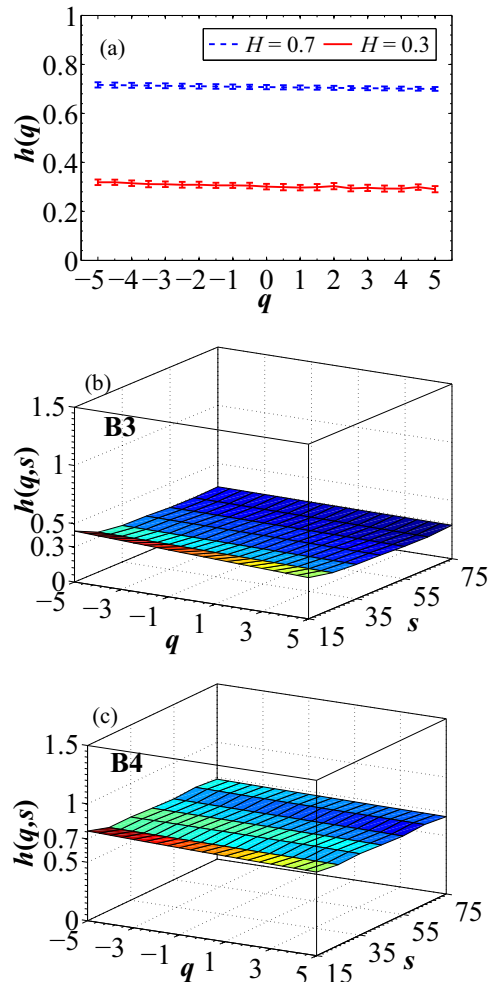

FIG. 6. Estimated multifractal long range correlation scaling exponents for the fGn surfaces B3 and B4 with given Hurst indices H. Notation as in Fig. 5.
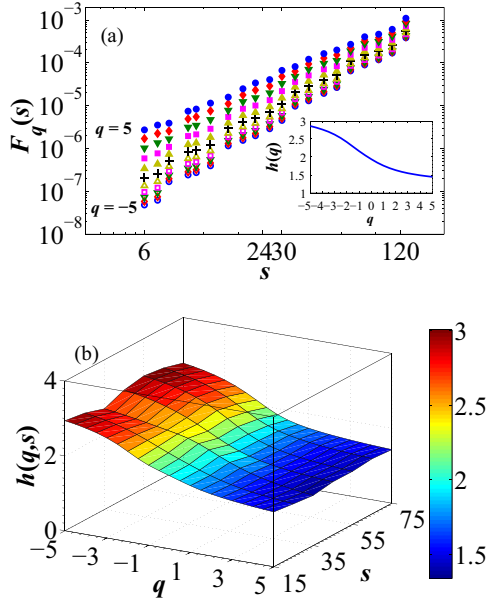
FIG. 7. Multifractal structure of the synthetic multifractal surface generated p model by with parameter $p = [0.1, 0.2, 0.3, 0.4]$. (a) is the fluctuation function $F_q(s)$ versus scale s calculated using 2D MF-DFA with kinds of q. Inset: corresponding $h(q)$ dependence. (b) is the Hurst surface for the synthetic surface in (a).

the right side of Fig. 1). Its properties are the reverse, i.e., it is monofractal at small scales and multifractal at large scales.

As expected, similar to the crossovers appeared in 1D case checked by the MMA [30], the coexistence of the measurements of monfractality and multifractality in those two surfaces produces crossovers, which suggests that the $h(q)$ changes over the varying scales. Figure 2(a) shows that the multifractality dominates in the small scale range (i.e., $s \in [6,24]$) and that monofractality dominates in the large ($s \in [30,120]$). In contrast, in Fig. 2(b) the horizontal red line in the subplot is the monofractality that dominates in the small

scale range, and the falling green curve is the multifractality that dominates in the large. Both of those indicate that the crossovers are caused by a change of the fractal properties with scale on the surfaces. We thus employ a surface of $h(q,s)$ to characterize the fractal properties instead of $h(q)$, which means that here we must use MMDFA instead of the standard MF-DFA. The fractal properties of A1 and A2 are depicted by the Hurst surfaces, shown in Figs. 3(a) and 3(b), respectively.

B. Testing for 2D synthetic surfaces

To test the validity of using 2D MMA on a 2D surface, we use MATLAB software FracLab 2.04 developed by INRIA to generate a fractional Brownian motion (fBm) function [15], a typical nonstationary signal. We also generate a fractional Gaussian noise (fGn) function [34], a classical stationary signal, using the mixed second partial derivatives of the 2D fBm [35]:

$$\frac{\partial^2}{\partial x \partial y} B_H(x,y) = [B_H(x,y) - B_H(x-1,y)]$$

$$-[B_H(x,y-1) - B_H(x-1,y-1)]. \quad (5)$$

Note that both of the fBm and fGn surfaces possess monofractal natures. Note also that the $h(q)$ of the fBm surface and fGn surface come in direct contact with the Hurst exponents. The relationship between the $h(q)$ and the Hurst exponent H for the fBm surface is $H = h(q) - 2$ and $H = h(q)$ for the fGn surface [33]. We set two H values, 0.3 and 0.7 [i.e., $h(q) = 2.3$ and 2.7 for the fBm surface; $h(q) = 0.3$ and 0.7 for the fGn surface], to generate the four monofractal surfaces of size 512×512 pixels, denoted B1, B2, B3, and B4, respectively (see Fig. 4). Figures 5 and 6 show the results of the four monofractal signals. Note that for every scale s we obtain flat Hurst surfaces at 0.3 [Figs. 5(b) and 6(b)] and 0.7 [Figs. 5(c) and 6(c)].

To further test the validity of using the 2D MMA method on a 2D surface, we use a multiplicative cascading process (Sec. III A) to generate a multifractal surface of size 512×512
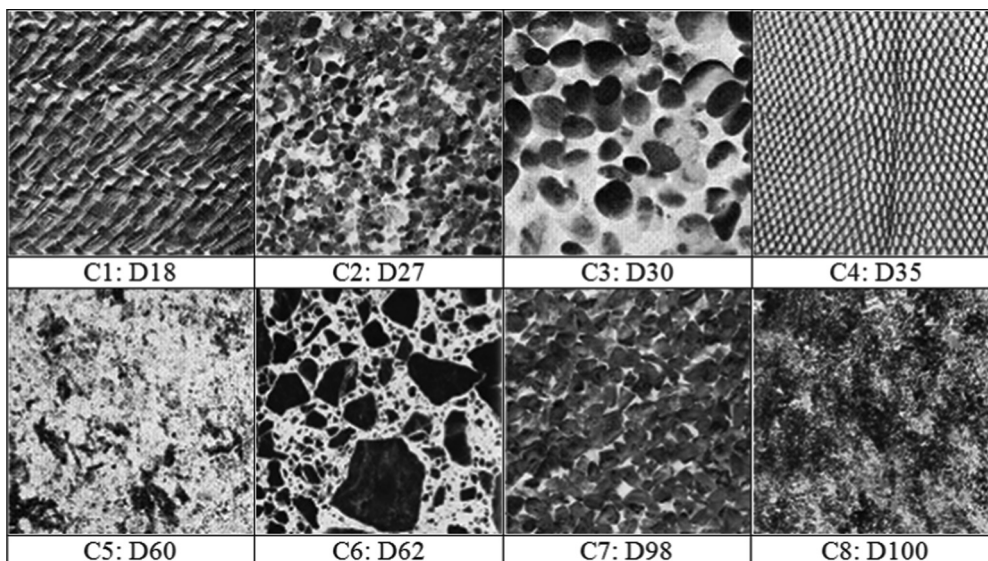

FIG. 8. Eight natural textures in Brodatz album.

TABLE I. The average of $h(2,s)$ over all the scales and $\Delta h(q,s)$ between the maximum and minimum of $h(q,s)$ calculated for the textures C1–C8 by 2D MMA with different combination {WL, SL}. The number in the parentheses of the first column is the number of scales for each WL, SL combination. The number in the parentheses beside the $h(2,s)$ is the standard deviation of the $h(2,s)$ over all the scales.

{WL,SL}	Observation	C1	C2	C3	C4	C5	C6	C7	C8
{2,4} (19)	$h(2,s)$	1.72(0.33)	1.91(0.27)	2.29(0.20)	1.09(0.56)	1.91(0.14)	2.07(0.24)	1.89(0.27)	1.87(0.05)
	$\Delta h(q,s)$	1.58	2.32	2.67	3.33	2.39	2.93	1.59	1.21
{2,6} (13)	$h(2,s)$	1.73(0.34)	1.91(0.28)	2.29(0.21)	1.10(0.58)	1.91(0.15)	2.08(0.25)	1.90(0.28)	1.88(0.05)
	$\Delta h(q,s)$	1.56	2.32	2.67	3.33	2.39	2.93	1.59	1.07
{2,10} (8)	$h(2,s)$	1.76(0.37)	1.94(0.30)	2.30(0.20)	1.13(0.64)	1.93(0.15)	2.10(0.27)	1.93(0.29)	1.89(0.05)
	$\Delta h(q,s)$	1.56	2.32	2.67	3.33	1.57	2.93	1.31	1.07
{4,4} (9)	$h(2,s)$	1.84(0.28)	2.01(0.23)	2.37(0.14)	1.18(0.58)	1.96(0.10)	2.14(0.19)	2.00(0.21)	1.87(0.03)
	$\Delta h(q,s)$	1.44	1.92	1.77	3.02	1.35	1.99	1.10	0.99
{4,6} (6)	$h(2,s)$	1.86(0.30)	2.03(0.24)	2.38(0.14)	1.21(0.62)	1.97(0.10)	2.16(0.21)	2.01(0.28)	1.87(0.03)
	$\Delta h(q,s)$	1.44	1.92	1.77	3.02	1.28	1.99	1.11	0.99
{4,10} (4)	$h(2,s)$	1.88(0.34)	2.03(0.28)	2.38(0.16)	1.26(0.70)	1.97(0.12)	2.18(0.25)	2.02(0.26)	1.88(0.03)
	$\Delta h(q,s)$	1.44	1.92	1.62	3.00	1.27	1.72	1.05	0.98

pixels. Figure 7 shows the multifractal structure of the 2D surface. Note that we have satisfying results because the shapes of $h(q,s)$ [Fig. 7(b)] on all available scales strongly resemble the standard shape of the multifractal $h(q)$ dependence [see insert plot in Fig. 7(a)]. Although the large fluctuations in $F_q(s)$ at negative q values causes slight fluctuations, we still get a multifractal property and an accurate estimate of the scaling exponent for the multifractal surface with the multiplicative cascading from the Hurst surface. These results indicate that the 2D MMA method can be used for a 2D surface.

C. Effect of moving windows length and sliding length

As mentioned above, window length (WL) and slide length (SL) can change the shape of $h(q,s)$ (the Hurst surface). Here we explore how the WL and SL affect the 2D MMA results for a 2D surface and determine the combination of {WL, SL} that yields the most accurate results. We focus our investigation on eight natural textures of 640×640 pixels, C1, C2, ..., C8, randomly chosen from the free Brodatz album [36] (see Fig. 8; their numbers of C1, C2, ..., C8 in our work and corresponding serial number in original Brodatz album are also shown below each figure). Once again, if the WL values are too large, we will not be able to observe variations in the local exponents. If they are too small, noise will bias the results. We investigate six {WL, SL} value combinations, {2, 4}, {2, 6}, {2, 10}, {4, 4}, {4, 6}, and {4, 10}. Figure 9 shows the dependence of the Hurst surfaces $h(q,s)$ calculated for texture image C1 using the six {WL, SL} value combinations. Many folds appear in the Hurst surface when the WL is small because there are huge fluctuations in the fitting slope $h(q,s)$. When the surface is too smooth (e.g., combination {4, 10}), the results produce less $F_q(s)$ information.

Table I displays the result of our calculations of $h(q = 2,s)$, the Hurst exponent, and $\Delta h(q,s)$, the multifractality strength, for the eight textures. Note that the number of scales differ with the {WL, SL} value combinations. Under the corresponding combinations there are 19, 13, 8, 9, 6, and 4 scales, respectively.
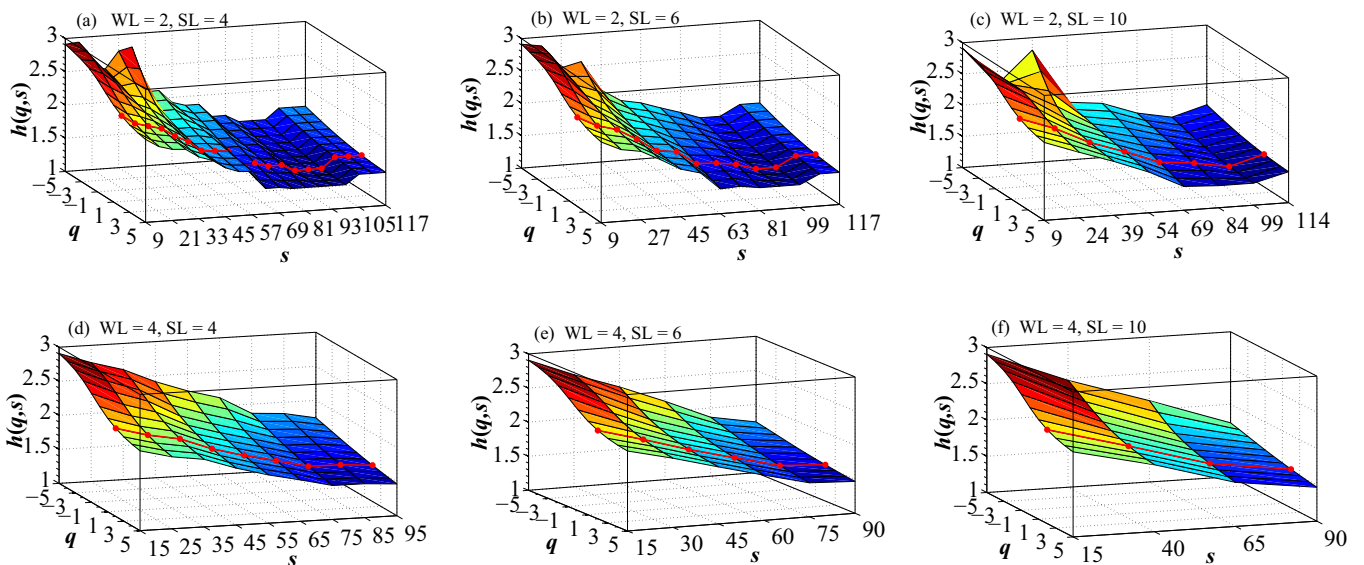

FIG. 9. Hurst surface $h(q,s)$ dependence calculated for the texture image C1 with different parameter combinations {WL, SL}. The red points correspond to $h(2,s)$.
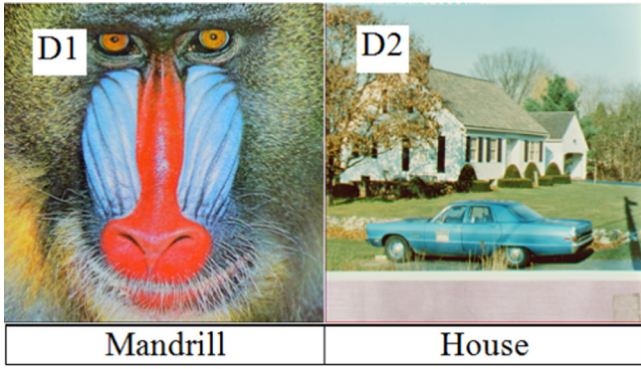
FIG. 10. Two images in the real world.

Note that Table I shows the standard deviation of the $h(2,s)$ over all the scales in the table. The results indicate the following:

(i) The WL is more critical than the SL when estimating the Hurst exponent, and the WL is the primary cause of the Hurst surface oscillation.

(ii) The $h(2,s)$ increases slightly with increasing WL. Conversely, the $\Delta h(q,s)$ sharply decreases with increasing WL. This indicates that increasing WL will enhance the long-term correlation of the gray surface somewhat, but will greatly seemingly weaken the obtained multifractal properties of the surface.

(iii) The standard deviation of the $h(2,s)$ is relatively small when WL is large and SL small, indicating that this combination produces more robust results. We thus suggest that 2D MMA use the {4, 4} combination for a 2D image.

D. Effect of noise

Noise is always present in the acquisition and transmission of real-world images, and thus it affects the 2D MMA results for a 2D surface. In Sec. III A we merged synthetic surfaces with random noise and found that noise can affect the multifractality or monofractality of the original synthetic surface at both small and large scales. Here we determine how noise affects 2D MMA results for real-world images. We choose two real-world images of size 512×512 pixels, "Mandrill" (D1) and "House" (D2), from the free USC-SIPI image database [37] (see Fig. 10). We add four common noises [38], (i) Gaussian noise with zero mean and variance of 0.01, (ii) salt and pepper noise with 4% density, (iii) Poisson noise with zero mean and variance of 0.04, and (iv) speckle noise, also with zero mean and variance of 0.04. Figure 11 shows the dependence of the Hurst surfaces $h(q,s)$ when WL = 4 and SL = 4 calculated for the D1 image when the four kinds of noise are added.

Figure 11 shows that when q is negative and the scale small, the $h(q,s)$ value is sharply altered and the Hurst surface of the original image differs greatly from the Hurst surface of the noised image. All noises except salt and pepper noise reduce the $h(q,s)$ value when q is negative and the scale small. This indicates that noises have more of an influence on segments with small fluctuations (when q is negative) than on segments with large fluctuations (when q is positive). To further explore how noise affects 2D MMA results at different scales, we calculate $h(2,s)$ for images D1 and D2 and for noised versions of D1 and D2 (see Fig. 12). Table II lists three key Hurst surface characteristics, $\max_{q,s}\{h(q,s)\}$, $\min_{q,s}\{h(q,s)\}$, and $\Delta h(q,s)$. Figure 12 shows detached lines when the scale is small, indicating that the noises strongly impact $h(2,s)$. When the scale is large, however, the properties of $h(2,s)$ are robust. This finding tells us how noise affects an image and enables us to use 2D MMA to analyze a noised image. Table II shows the difference in degree of influence each noise has on D1 and D2. In general, the noises reduce the $h(q,s)$ values in both images. All noises except salt and pepper noise strengthen the multifractality in D1 and weaken it in D2.
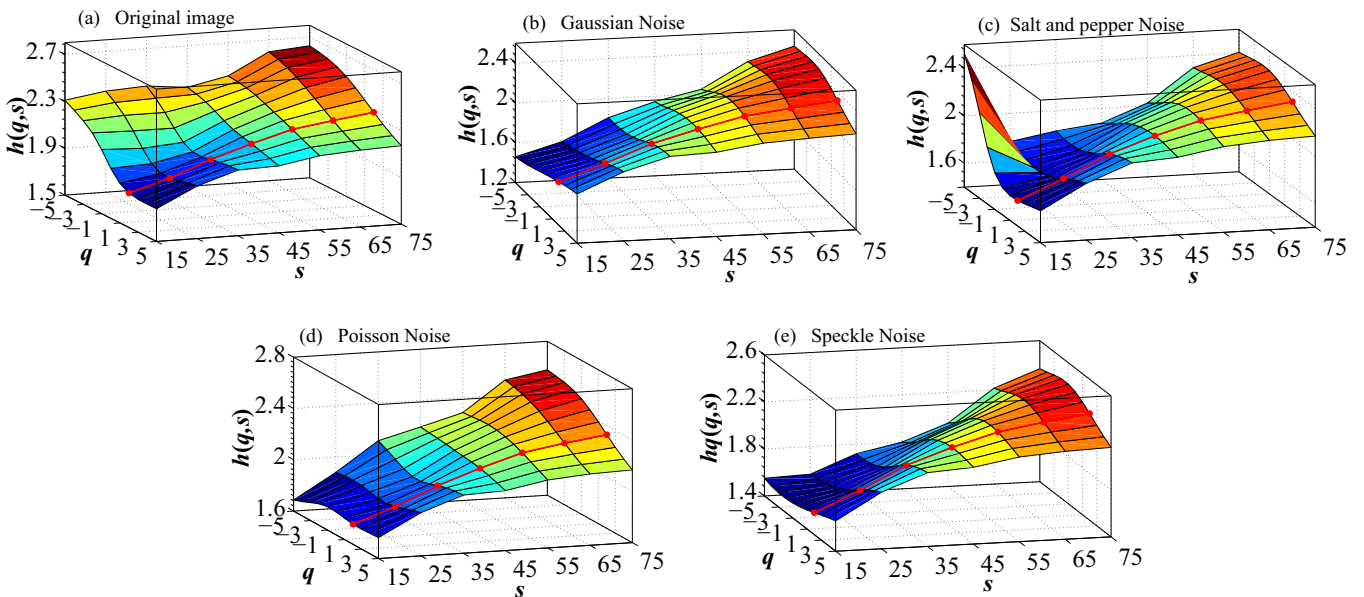

FIG. 11. Hurst surface $h(q,s)$ dependence calculated for the image D1 added on different noises. The red points corresponds to $h(2,s)$. The presented results have been averaged over 20 realizations of the test series.

TABLE II. The maximum and minimum of $h(q,s)$ and $\Delta h(q,s)$ calculated for the original images and noised images. The presented results have been averaged over 20 realizations of the test series.

Noise	Image D1			Image D2		
	$\max\limits_{q,s}\{h(q,s)\}$	$\min\limits_{q,s}\{h(q,s)\}$	$\Delta h(q,s)$	$\max\limits_{q,s}\{h(q,s)\}$	$\min\limits_{q,s}\{h(q,s)\}$	$\Delta h(q,s)$
Original	2.6258	1.7775	0.8483	3.3304	1.9465	1.3839
Gaussian	2.4625	1.4581	1.0044	2.3673	1.2101	1.1572
Salt and pepper	2.5218	1.6077	0.9141	4.0842	1.3887	2.6955
Poisson	2.5777	1.6866	0.8911	2.4660	1.3307	1.1353
Speckle	2.4185	1.5196	0.8989	2.2875	1.1974	1.0901

To determine whether noise affects the estimation accuracy of $h(q,s)$, shown as the fitting error between fluctuation function $F_q(s)$ and scale s in a double-log plot, and to evaluate the error, we define a distance error DE function

$$\text{DE} = \frac{1}{n}\sqrt{\sum_{i=1}^{n}\frac{(kx_i + c - y_i)^2}{(1+k)^2}}, \qquad (6)$$

where $y = kx + c$ is the fitted line, y is $\log F_q(s)$, x is $\log s$, and n is the number of points in each scale. Figure 13 shows the average DE over the all scales for images D1 and D2. All of the DE are less than 0.01 for D1 and less than 0.02 for D2, indicating that the noise immunity of 2D MMA is robust.

We thus conclude that noise does not destroy the efficiency of 2D MMA but in varying degrees does impact the $h(2,s)$ results. Because varying the intensity of a noise changes its

impact on the results, we apply a varying peak signal-to-noise ratio (PSNR) to images D1 and D2. We add Gaussian noise with six PSNR values (27 to 32 dB at 1 dB steps) and salt-and-pepper noise with six PSNR values (36 to 46 dB at 2 dB steps) to images D1 and D2. Figures 13 and 14 show the Hurst surface $h(q,s)$ dependence calculated for image D1 with Gaussian noise and salt and pepper noise added at different PSNR values. Figure 16 shows the average distance errors. Figures 14 and 15 show that the shape of the Hurst surface is basically unchanged, and Fig. 16 shows that the all of the DE are less than 0.012. Those results indicate that the performance of 2D MMA is robust.

To quantify the impact of the two kinds of noise with different PSNR values on different scales using 2D MMA, we calculate the relative error of the $h(2,s)$ between the noisy
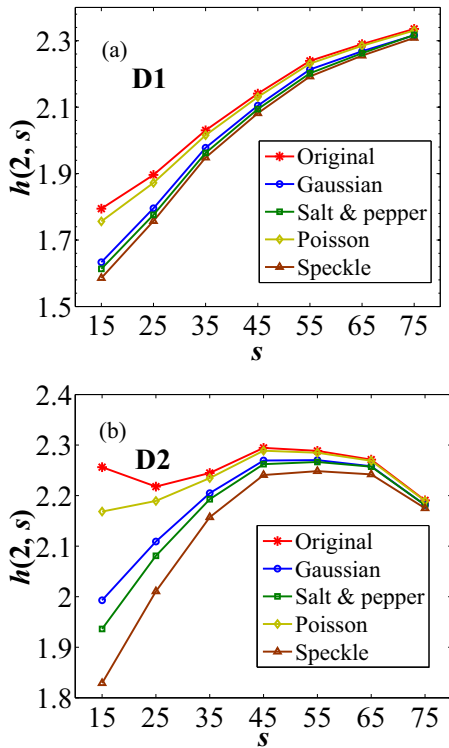

FIG. 12. The $h(2,s)$ calculated for the images D1 and D2 added on different noises. The presented results have been averaged over 20 realizations of the test series.
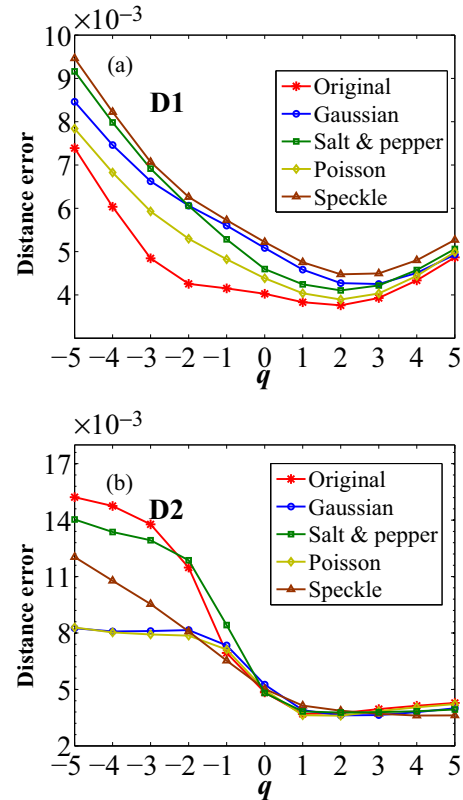

FIG. 13. Average distance error of $h(q,s)$ over all the scales calculated for the kinds of noised images. The presented results have been averaged over 20 realizations of the test series.
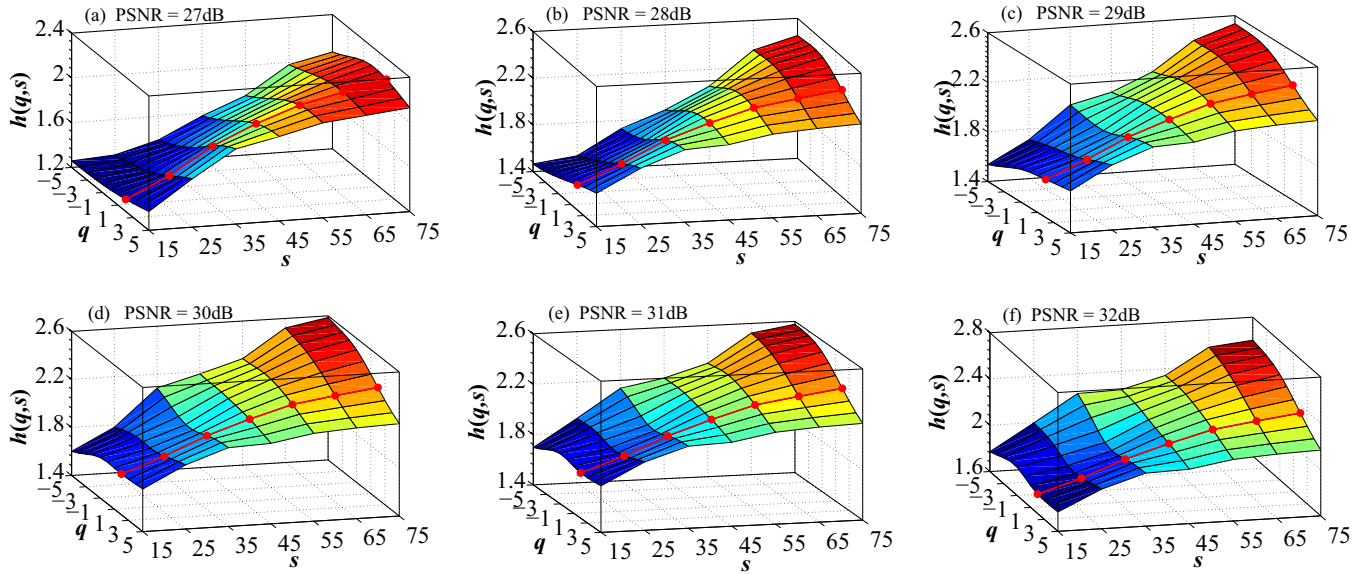
FIG. 14. Hurst surface $h(q,s)$ dependence calculated for the image D1 added on Gaussian noises with different PSNR. The red points corresponds to $h(2,s)$. The presented results have been averaged over 20 realizations of the test series.

images and the original images (see Fig. 17). As in Table II, we include the original values of the $\max_{q,s}\{h(q,s)\}$, $\min_{q,s}\{h(q,s)\}$, and $\Delta h(q,s)$ in Tables III and IV. From them we conclude the following:

(i) For both kinds of noise, the relative error increases with the noise intensity and the PSNR decreases. This occurs when the scale is small, e.g., as in initial scale range $s \in [6,24]$ and the following scale range $s \in [10,40]$, but the relative error is $< 10\%$ when the scale exceeds $s \in [14,56]$. This indicates that when the scale is large $h(2,s)$ is more stable and less affected by noise. 2D MMA can thus be used to calculate this exponent for a 2D image when the scale is large.

(ii) Increasing the Gaussian noise decreases the $h(q,s)$ value in both images but increases the degree of multifractality. In the D1 image $\Delta h(q,s)$ increases as the noise increases. In the D2 image $\Delta h(q,s)$ decreases as the noise increases. We also find that increasing the Gaussian noise decreases the long-term correlation of the gray surface.

(iii) In the D1 image, increasing the salt and pepper noise decreases the $h(q,s)$ values and increases the $\Delta h(q,s)$ values. In the D2 image, when q is negative the $\max_{q,s}\{h(q,s)\}$ values increase and the PSNR values decrease. When q is positive, the reverse occurs. When using standard MF-DFA the negative q values correspond to those segments of the surface that have
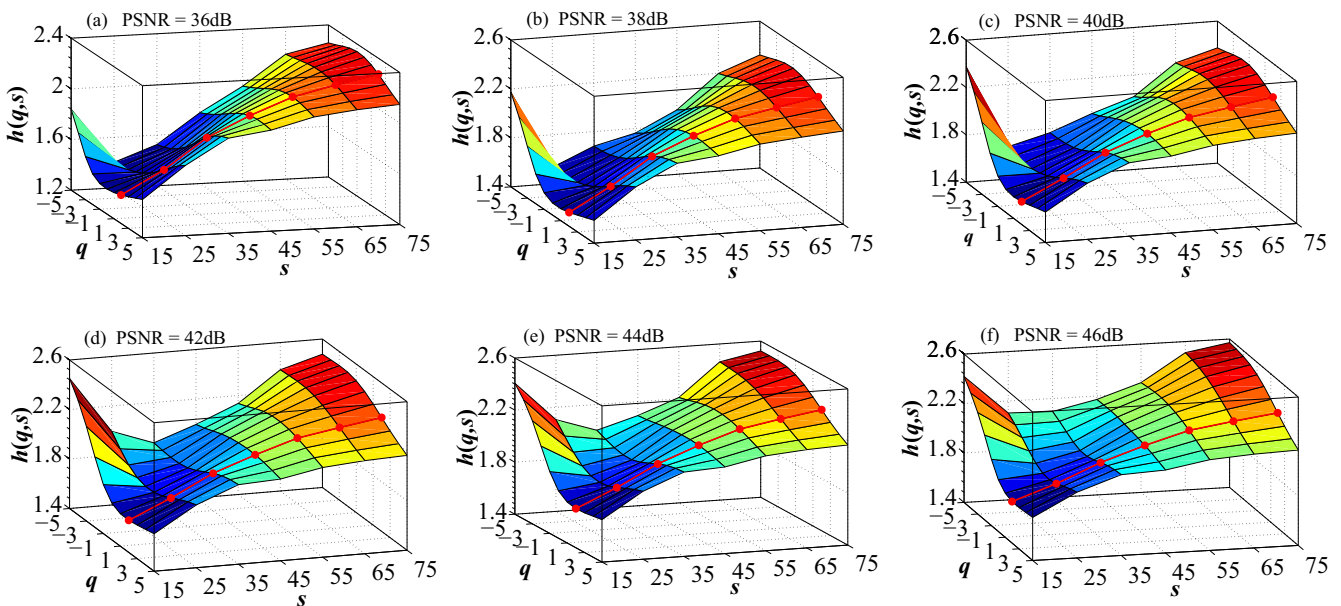

FIG. 15. Hurst surface $h(q,s)$ dependence calculated for the image D1 added on salt and pepper noises with different PSNR. The red points corresponds to $h(2,s)$. The presented results have been averaged over 20 realizations of the test series.
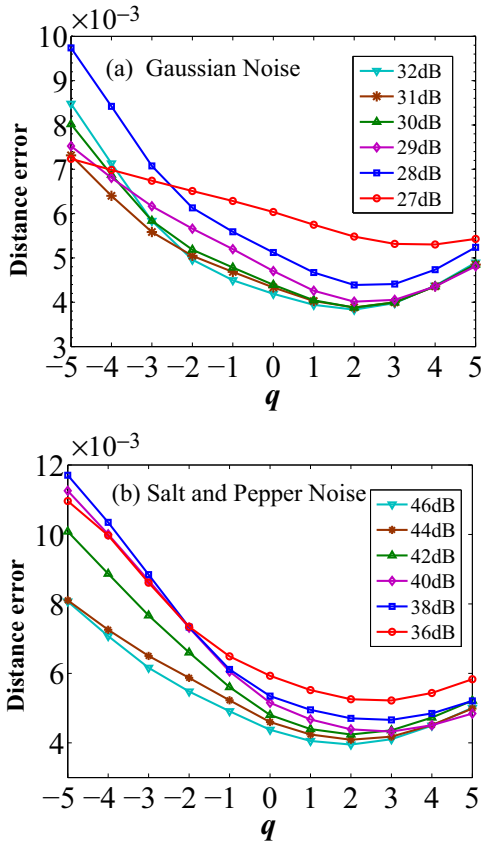
FIG. 16. Average distance error of $h(q,s)$ over all the scales calculated for the noised image of D1 with different PSNR. The presented results have been averaged over 20 realizations of the test series.
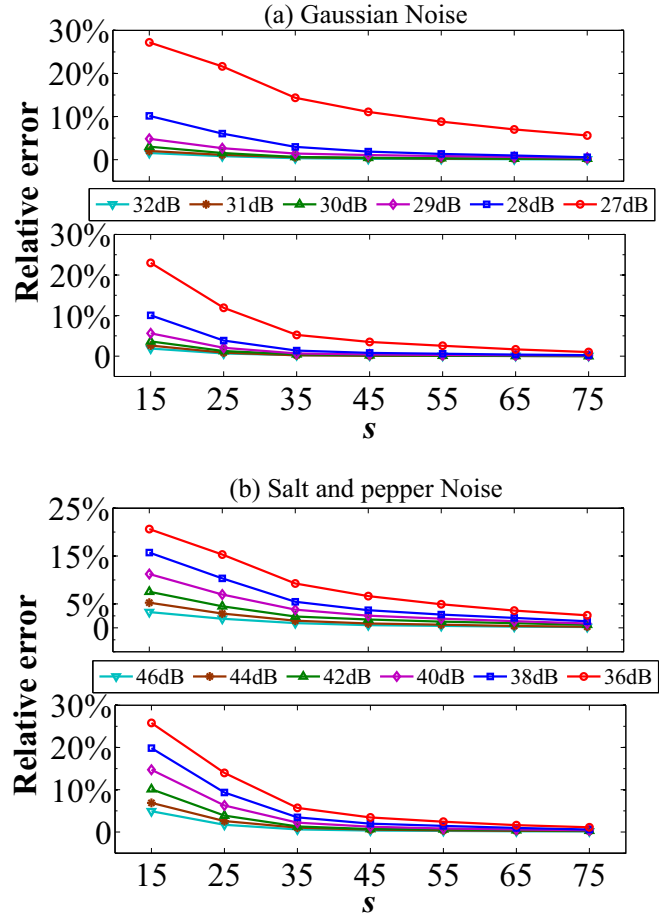

FIG. 17. Relative error of the Hurst exponent $h(2,s)$ calculated for the noised images of D1 and D2 with different PSNR. The upper one denotes the image D1; the bottom one denotes the image D2. The presented results have been averaged over 20 realizations of the test series.

small fluctuations. Because the negative exponential effect increases the influence of small fluctuations, they function as noise and increases the $\max_{q,s}\{h(q,s)\}$ values too quickly. This may bias the results. Thus the results when $q < 0$ should be viewed with suspicion. The $\min_{q,s}\{h(q,s)\}$ values apply only to salt and pepper noise on the D2 image, and their decrease as noise increases is similar to that found in the D1 image.

IV. CONCLUSIONS

Advances in statistical physics have strongly contributed to research on the multifractal scaling of fluctuations on a 2D

surface. Although the MF-DFA technique in its 2D version has become a powerful tool in surface analysis, standard MF-DFA results are a univariate function of q at a constant scale s, and thus much information disappears. To recover the missing information produced at different scales, we have applied 2D multifractal detrended fluctuation analysis (2D MMA) to investigate the fractal properties of 2D surfaces and have used a spectrum of local Hurst exponents: $h(q,s)$ (Hurst surface).

TABLE III. The values of maximum and minimum of $h(q,s)$ and $\Delta h(q,s)$ calculated for the Gaussian noises images with varying PSNR. The presented results have been averaged over 20 realizations of the test series.

PSNR	Image D1			Image D2		
	$\max_{q,s}\{h(q,s)\}$	$\min_{q,s}\{h(q,s)\}$	$\Delta h(q,s)$	$\max_{q,s}\{h(q,s)\}$	$\min_{q,s}\{h(q,s)\}$	$\Delta h(q,s)$
32	2.6013	1.7610	0.8403	2.6388	1.3186	1.3202
31	2.6073	1.7190	0.8884	2.5732	1.3030	1.2702
30	2.5765	1.6397	0.9368	2.5266	1.2851	1.2415
29	2.5611	1.5647	0.9964	2.4561	1.2394	1.2167
28	2.4595	1.4260	1.0335	2.3870	1.2464	1.1406
27	2.2210	1.2557	0.9654	2.2745	1.1789	1.0956

TABLE IV. The values of maximum and minimum of $h(q,s)$ and $\Delta h(q,s)$ calculated for the salt and pepper noise images with varying PSNR. The presented results have been averaged over 20 realizations of the test series.

PSNR	Image D1			Image D2		
	$\max\limits_{q,s}\{h(q,s)\}$	$\min\limits_{q,s}\{h(q,s)\}$	$\Delta h(q,s)$	$\max\limits_{q,s}\{h(q,s)\}$	$\min\limits_{q,s}\{h(q,s)\}$	$\Delta h(q,s)$
46	2.5713	1.7343	0.8370	3.3477	1.7762	1.5714
44	2.5250	1.7002	0.8248	3.3435	1.6119	1.7316
42	2.4869	1.6594	0.8275	3.9429	1.4891	2.4538
40	2.4354	1.5818	0.8536	4.1272	1.3602	2.7670
38	2.4002	1.4966	0.9036	4.0235	1.2696	2.7539
36	2.3408	1.3967	0.9441	4.1439	1.2440	2.8999

The 2D MMA method allows us to analyze the multifractal properties of the 2D surface at multiple scales.

We first examine the validity of the 2D MMA method for a 2D surface. We use two merged surfaces, amalgamated multifractal measure and uniform distribution random variables, that cause the monofractality and multifractality coexist, and find that the 2D MMA method can capture the properties in both small scales and large. We use the fBm model and the fGn model with given Hurst exponents to generate two synthetic surfaces and obtain useful results on the flat Hurst surfaces produced by the 2D MMA, located at the Hurst exponents. We generate a synthetic surface using multiplicative cascading and find that all of the $h(q,s)$ values in every scale s exhibit the standard shape of multifractal $h(q)$ dependence, indicating that 2D MMA can accurately estimate Hurst exponents on 2D surfaces. These results also indicate that 2D MMA can both estimate generalized Hurst exponents for a 2D surface and quantify fractal properties at different scales.

We next measure how moving window length (WL) and sliding length (SL) affect the 2D MMA method. We perform 2D MMA using six combinations of {WL, SL} on eight natural textures selected from the Brodatz album and find that WL causes the $h(q,s)$ to fluctuate and that SL does not. We determine that combination {4, 4} used with 2D MMA on a 2D image produces the most stable behavior in $h(2,s)$.

In the final section we examined the effect of noise. We introduce four kinds of noise into two real-world images and find that they affect $h(2,s)$ only at small scales. We also find that the long-term correlation properties in the two images decrease when noise, either Gaussian or salt and pepper, is increased.

In summary, our findings are of great importance when applying 2D MMA to 2D surfaces.

ACKNOWLEDGMENTS

[1] B. B. Mandelbrot and J. W. V. Ness, SIAM Rev. **10**, 422 (1968).

[2] B. B. Mandelbrot, Sci. Am. **280**, 70 (1999).

[3] A. P. Pentland, IEEE Trans. Pattern Analy. Mach. Intell. **PAMI-6**, 661 (1984).

[4] R. Lopes, P. Dubois, I. Bhouri, M. H. Bedoui, S. Maouche, and N. Betrouni, Pattern Recogn. **44**, 1690 (2011).

[5] L. Yu and D. W. Qi, Wood Sci. Technol. **45**, 511 (2011).

[6] D. Riccio and G. Ruello, IEEE Trans. Geosci. Remote Sensing **53**, 3803 (2015).

[7] C.-K. Peng, S. V. Buldyrev, S. Havlin, M. Simons, H. E. Stanley, and A. L. Goldberger, Phys. Rev. E. **49**, 1685 (1994).

[8] P. Oświęcimka, J. Kwapień, and S. Drożdż, Phys. Rev. E. **74**, 016103 (2006).

[9] J. W. Kantelhardt, S. A. Zschiegner, E. Koscielny-Bunde, S. Havlin, A. Bunde, and H. E. Stanley, Physica A **316**, 87 (2002).

[10] F. Wang, G. P. Liao, X. Y. Zhou, and W. Shi, Nonlinear Dynamic **72**, 353 (2013).

[11] F. Wang, G. P. Liao, J. H. Li, X. C. Li, and T. J. Zhou, Physica A **392**, 5723 (2013).

[12] L. Hedayatifar, M. Vahabi, and G. R. Jafari, Phys. Rev. E **84**, 021138 (2011).

[13] M. S. Movahed, G. R. Jafari, F. Ghasemi, S. Rahvar, and M. R. R. Tabar, J. Stat. Mech.: Theory Exp. (2006) P02003.

[14] Y. Zhou and Y. Leung, J. Stat. Mech.: Theory Exp. (2010) P06021.

[15] G. F. Gu and W. X. Zhou, Phys. Rev. E **74**, 061104 (2006).

[16] F. Wang, L. Wang, and R. B. Zou, Chaos **24**, 033127 (2014).

[17] F. Wang, Z. S. Li, and G. P. Liao, Intl. J. Pattern Recogn. Artificial Intell. **28**, 1455005 (2014).

[18] F. Wang, Z. S. Li, and J. W. Li, Appl. Surf. Sci. **322**, 116 (2014).

[19] R. P. Yadav, S. Dwivedi, A. K. Mittal, M. Kumar, and A. C. Pandey, Appl. Surf. Sci. **261**, 547 (2012).

[20] F. Wang, J. W. Li, W. Shi, and G. P. Liao, J. Appl. Phys. **114**, 214905 (2013).

[21] F. Wang, D. W. Liao, J. W. Li, and G. P. Liao, Plant Methods **11**, 12 (2015).

[22] Y. E. Yu, F. Wang, and L. L. Liu, Appl. Surf. Sci. **356**, 266 (2015).

[23] E. J. Ge and Y. Leung, J. Geograph. Syst. **15**, 115 (2013).

[24] H. E. Stanley, L. A. N. Amaral, A. L. Goldberger, S. Havlin, P. C. Ivanov, and C. K. Peng, Physica A **270**, 309 (1999).

[25] D. Grech and Z. Mazur, Physica A **336**, 133 (2004).

[26] J. C. Echeverría, M. S. Woolfson, J. A. Crowe, B. R. Hayes-Gill, G. D. H. Croaker, and H. Vyas, Chaos **13**, 467 (2003).

[27] R. B. Govindan, J. D. Wilson, H. Preißl, H. Eswaran, J. Q. Campbell, and C. L. Lowery, Physica D **226**, 23 (2007).

[28] P. Castiglioni, G. Parati, C. Lombardi, L. Quintin, and M. D. Rienzo, Biomedizin. Tech./Biomed. Eng. **56**, 175 (2011).

[29] P. Castiglioni, G. Parati, M. D. Rienzo, R. Carabalona, A. Cividjian, and L. Quintin, J. Physiol. **589**, 355 (2011).

[30] J. Gierałtowski, J. J. Żebrowski, and R. Baranowski, Phys. Rev. E **85**, 021915 (2012).

[31] J. Wang, P. J. Shang, and X. R. Cui, Phys. Rev. E **89**, 032916 (2014).

[32] J. Gieraltowski, D. Hoyer, F. Tetschke, S. Nowack, U. Schneider, and J. Żebrowski, Auton. Neurosci. **178**, 29 (2013).

[33] Y. Zhou, Y. Leung, and Z. G. Yu, Phys. Rev. E **87**, 012921 (2013).

[34] Y. Xia, D. G. Feng, and R. C. Zhao, IEEE Trans. Image Proc. **15**, 614 (2006).

[35] D. R. McGaughey and G. J. M. Aitken, Physica A **311**, 369 (2002).

[36] P. Brodatz, *Textures: A Photographic Album for Artists and Designers* (Dover, New York, 1966).

[37] http://sipi.usc.edu/database/database.php.

[38] J. Sklansky and V. Gonzalez, Pattern Recognition **12**, 327 (1980).